Computational fluid-structure interaction analysis of the end-to-side radio-cephalic arteriovenous fistula

Fabio Marcinnò [a], Christian Vergara [b,*], Luca Giovannacci [c], Alfio Quarteroni [d,a], Giorgio Prouse [c]

[a] *Institute of Mathematics, École Polytechnique Fédérale de Lausanne, Lausanne, Switzerland*
[b] *LaBS, Dipartimento di Chimica, Materiali e Ingegneria Chimica "Giulio Natta", Politecnico di Milano, Milan, Italy*
[c] *Centro Vascolare Ticino, EOC-Ente Ospedaliero Cantonale, Ticino, Switzerland*
[d] *MOX, Dipartimento di Matematica, Politecnico di Milano, Milan, Italy*

ARTICLE INFO

ABSTRACT

Background and Objective: In the current work, we present a descriptive fluid-structure interaction computational study of the end-to-side radio-cephalic arteriovenous fistula. This allows us to account for the different thicknesses and elastic properties of the radial artery and cephalic vein.
Methods: The core of the work consists in simulating different arteriovenous fistula configurations obtained by virtually varying the anastomosis angle, i.e. the angle between the end of the cephalic vein and the side of the radial artery. Since the aim of the work is to understand the blood dynamics in the very first days after the surgical intervention, the radial artery is considered stiffer and thicker than the cephalic vein.
Results: Our results demonstrate that both the diameter of the cephalic vein and the anastomosis angle play a crucial role to obtain a blood dynamics without re-circulation regions that could prevent fistula failure.
Conclusions: When an anastomosis angle close to the perpendicular direction with respect to the radial artery is combined with a large diameter of the cephalic vein, the recirculation regions and the low Wall Shear Stress (WSS) zones are reduced. Conversely, from a structural point of view, a low anastomosis angle with a large diameter of the cephalic vein reduces the mechanical stress acting on the vessel walls.

1. Introduction

In the United States in 2019, about 130000 individuals were newly registered as having end-stage renal disease (ESRD) which represented an increase by 2.7% from the previous year and by 15.8% from a decade ago [52]. ESRD occurs when the kidneys have lost the ability to filter blood [3]. In the majority of cases, the problem is faced using hemodialysis, which is performed through a mechanical device called dialyser which emulates the function of the kidneys. To perform efficiently, the dialyzer needs a high blood flow, therefore the creation of a dedicated vascular access (VA) becomes mandatory [19].

Nowadays, the most efficient VA available for hemodialysis is represented by the native vessel arteriovenous fistula (nAVF) involving a connection between an artery and a vein at the most distal site possible [16,21]. In particular, the end-to-side radio-cephalic arteriovenous fistula (RCAVF) is the first choice for a native vessel VA [51] and it was introduced by Brescia and Cimino, in 1966 [14].

In the RCAVF, the end segment of the cephalic vein is anastomosed onto the side of the radial artery, as a consequence the former remodels its vessel structure, augmenting the wall thickness and improving its mechanical stiffness due to the increased flow and pressure originating from the arterial circulation. This process is called fistula maturation and it is essential to obtain a stable and reliable vascular access to the vein. Unfortunately, the main problem consists in a high rate of fistula maturation failure, approximately between 30% and 70% [51,2]. The failure is due to several complications strongly associated with a non-physiological structural remodeling of the cephalic vein, causing venous intimal hyperplasia (IH) leading to stenosis and thrombosis [22,19,37]. Concerning RCAVFs, there are typically two physiologic situations arising after creation of the AVF, the second one being the more frequent:

• RCAVF: with one inlet (the proximal radial) and two outlets (the cephalic vein and the distal radial artery);

---

* Corresponding author.
E-mail addresses: fabio.marcinno@epfl.ch (F. Marcinnò), christian.vergara@polimi.it (C. Vergara), luca.giovannacci@eoc.ch (L. Giovannacci), alfio.quarteroni@polimi.it (A. Quarteroni), giorgio.prouse@eoc.ch (G. Prouse).

- RCAVF-SS (steal syndrome): with two inlets (the distal and the proximal radial artery) and one outlet (the cephalic vein). In this context, blood steal occurs, i.e. a retrograde flow coming from the distal radial artery is generated by the lower resistance of the cephalic vein [51,19],

where proximal artery refers to the tract of the artery closer to the heart, while distal artery to the one after the anastomosis region (bifurcation), i.e. more distant from the heart.

The usefulness of the computational methods in hemodynamics has been largely demonstrated [33,57], especially in analyzing critical regions such as bifurcations and complex geometric conditions (for example, stenosis or aneurysms) [47,55,44,46,9]. Since the disturbed hemodynamics at the anastomosis region, due to the unnatural path and to the artero-venous mismatch in wall thickness and elastic properties, plays a fundamental role in inducing the cited complications [19], numerical methods have been applied to analyze the hemodynamics of AVFs in the last 20 years.

Concerning the RCAVF-SS case, in [72] the author proposes a fluid-structure interaction (FSI) in patient-specific situations, where both the vessel wall of the radial artery and cephalic vein have the same thickness and stiffness properties. The concept of critical energy loss rate (CEL) referring to the maximum allowable energy loss rate in AVF is introduced. In [68], the authors perform a computational fluid dynamics (CFD) study exploiting the Large Eddy Simulation (LES) turbulence model to assess the best anastomosis angle, the one that minimizes oscillating shear index (OSI) and turbulent regions. In [13], the authors, through CFD simulations, compare the impact of an external support device against conventional surgical technique. They find that the device is able to maintain an optimal anastomosis angle promoting a more regular blood velocity pattern and stable morphology.

Considering FSI studies for the RCAVF case, in [23] the influence of the wall compliance on the hemodynamics of a patient-specific geometry is studied; the numerical results demonstrate that the cephalic vein is subjected to values of WSS two times higher than physiological level. In [65], the hemodynamics of an idealized geometry is studied, where the artery bed and heel of the AVF seem to be a susceptible area for IH; the authors find abnormal values of the Von-Mises stress at the anastomosis region. In [23,65], the authors assume different thicknesses for the vessel walls, and the cephalic vein stiffer than the radial artery after AVF maturation is achieved.

Other computational studies are focused on the brachio-cephalic arteriovenous fistula (BCAVF); this configuration has 1 inlet (the proximal brachial artery) and 2 outlets (the distal brachial artery and the cephalic vein). In [21], the results of the FSI are validated against magnetic resonance imaging (MRI) data. A region of high WSS is present at the toe of the anastomosis while a high OSI is found at the heel of the anastomosis. In [49], the BCAVF geometry is reconstructed from a 3D ultrasound scan. The authors find very large time-averaged wall shear stresses (TAWSS) at the anastomosis region. In [40], the results of patient-specific FSI are validated against the phase-contrast magnetic resonance angiography (PC-MRA) showing good agreement. In [12], the CFD analysis of the BCAVF is carried out. Owing to the use of the LES method, the zone of anastomosis is found to be characterized by a high-frequency disturbed flow. From the same group, in [11] the authors explore the feasibility of coupling a contrast-free MRI protocol with high-resolution computational fluid dynamics (HR-CFD) to relate the hemodynamic changes to vascular wall remodeling occurring during fistula maturation.

In some cases adequate native vessels may not be available for an AVF, especially in elderly women and in diabetic patients. In these cases, a possible alternative is the arteriovenous graft (AVG); this surgical intervention consists in creating a connection between the arterial and the venous circulation using a synthetic graft [7]. We refer to [7], for an immersed boundary formulation for the blood-flow graft-vein interaction, where the authors find that the WSS values on the graft are significantly greater than those on the vein. In [50], the authors perform a FSI simulation of a modular valve device in the context of AVG in order to find an efficient compromise between the vascular access during hemodialysis and the re-creation of a physiological circulation pattern.

In the present work, we propose a pulsatile descriptive computational FSI study for patient-specific end-to-side RCAVF-SS, parametrized on the anastomosis angle, to assess the influence of the latter on hemodynamics and on structural quantities, which are relevant for the RCAVF-SS failure. The choice of FSI is motivated by the need to distinguish between the artery and vein thickness and elastic properties, a fundamental feature to obtain realistic results. In particular, we study two patients and, by virtually varying the anastomosis angle, we propose three different geometric configurations for each patient. The work focuses on the first days immediately after the surgical intervention, i.e. when the radial artery and the cephalic vein still feature substantial differences in the stiffness and geometric properties.

The novelty of the paper consists in the inclusion of artery-venous elastic and wall thickness mismatches in an RCAVF-SS FSI study with different anastomosis angles. Moreover, for the first time we focus on the first days after the intervention, which are believed to be the most relevant in determining the conditions which may favor fistula failure [62].

The work is organized as follows. In Sec. 2, we describe the pre-processing for the generation of the fluid and structure grids. In Sec. 3, the mathematical model of the FSI is described. In Sec. 4, we report the input data and the discussion on fluid and structure numerical results. Here, we also present the limitations. Finally, in Sec. 5, we briefly summarize the conclusions of our work.

2. Pre-processing and mesh generation

In this work, two patients, P1 and P2, who underwent fashioning of end-to-side radio-cephalic AVF with a 40° and 70° angle respectively, are analyzed using an FSI computational model. The geometric reconstructions of the lumen are obtained from Echo-Color Doppler (ECD) acquisitions given by the EOC - Ente Ospedaliero Cantonale, Lugano, Switzerland, Divisions of Vascular Surgery and Angiology. All data and images are fully anonymised and the present study is approved by the local Ethics Committee. The 3D lumen surfaces are acquired from a previous CFD work of the group, see [68]. The structure domain is then generated for each patient by means of an extrusion of the 3D fluid domain through the use of the Vascular Modeling Toolkit (VMTK) [5]. Regarding the thickness τ of the vessel walls, we use $\tau_V = 0.1$ mm (suitable literature range 0.09 ± 0.01 mm) [38] for the cephalic vein and $\tau_A = 0.3$ mm (suitable literature range 0.28 ± 0.05 mm) [45] for the radial artery.

Subsequently, the anastomosis angle is virtually varied and three different configurations for each patient are analyzed: 20°, 40°, 60° for P1 ($P1-20$, $P1-40$, $P1-60$) and 30°, 50°, 70° for P2 ($P2-30$, $P2-50$, $P2-70$). In Fig. 1, we depict a generic angle ϑ for the configurations of P1 and P2. The arterial segments considered for P1 and P2 are 160 mm and 165 mm long, respectively; the anastomosis region (i.e. where the vein is sawn to the artery) has a length in the range of 15-20 mm, see Fig. 2, above, blue region. Moreover, both the distal and proximal arteries are co-planar with the vein.

The generation of the tetrahedral computational meshes is achieved using VMTK. In particular, the fluid mesh is obtained starting from the 3D reconstructed lumen surfaces with an average space discretization parameter $h = 0.5$ mm, with a boundary layer (BL) composed of three heterogeneous layers, where the one nearest to the wall has a thickness of 0.12 mm; the dimension of the other two internal layers increases by a factor of 25% compared to the previous one. The structure mesh is generated by the combined use of VMTK, MATLAB [48], and Gmsh [39]; it is composed of three layers with a total thickness of 0.1 mm
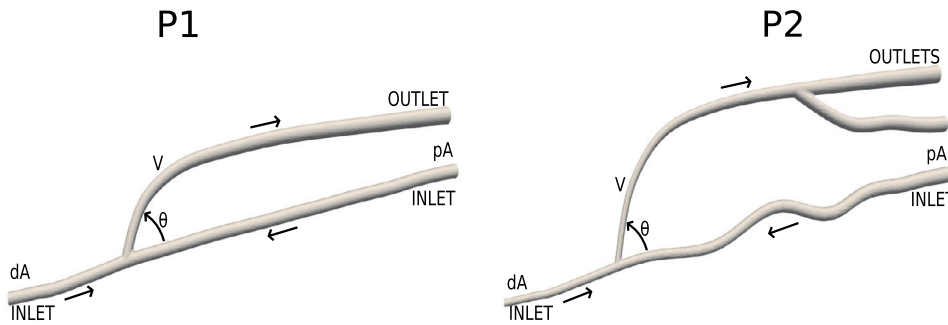
Fig. 1. Computational geometry for a generic anastomosis angle ϑ of P1 (left) and P2 (right). The arrows indicate the direction of the blood flow. pA= proximal artery, dA= distal artery, V= vein.

Table 1
Convergence test for the fluid and structure grids of P1-20: The relative errors for TAWSS and TAVMS, computed comparing the values with a reference solution, are reported. In parenthesis the number of elements of the grids and the average space discretization steps.

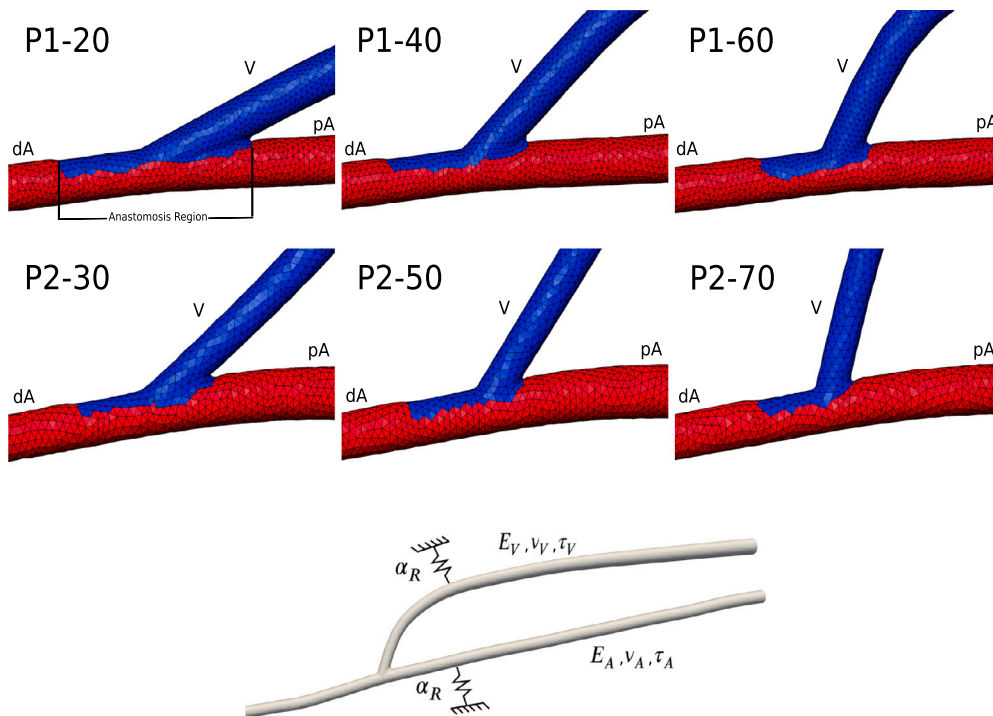| P1-20	Coarse (350k, 0.8 mm)	Medium (500k, 0.5 mm)	Fine (1150k, 0.1 mm)
Fluid mesh	7.6%	4.1%	2.7%
P1-20	Coarse (100k, 0.2 mm)	Medium (190k, 0.1 mm)	Fine (360k, 0.05 mm)
Structure mesh	7.3%	3.8%	2.5%

Fig. 2. Top: Computational structure meshes. The blue region represents the cephalic vein while the red one the radial artery. Bottom: Structural parameters. E_A is the artery Young's modulus, E_V is the vein Young's modulus, ν_A is the artery Poisson's coefficient, ν_V is the vein Poisson's coefficient, τ_A and τ_V are the thickness of the artery and vein walls, respectively, α_R is the Robin surrounding tissue coefficient. pA= proximal artery, dA= distal artery, V= vein.

(cephalic vein) and 0.3 mm (radial artery) each, and it is conforming at the interface to the fluid one [31].

The correctness of such meshes is the result of mesh convergence tests performed on both the structure and fluid meshes. In Table 1, we report the values of the relative errors of the time-averaged wall shear stress (TAWSS) for the fluid mesh and the time-averaged Von-Mises stress (TAVMS) for the structure mesh. The convergence is checked by means of a coarse, a medium, and a fine mesh; the error is computed comparing the values with a reference solution constructed with the Richardson extrapolation [61]. As output of such convergence tests, in all the numerical experiments reported in Sec. 4 we use the medium meshes since they are able to keep the error w.r.t. the previous ones to about 4%, which is a good compromise between accuracy and computational cost of the simulations.

At the top of Fig. 2, we depict the structure meshes in the three configurations for each patient. We also highlight by different colors the arterial and vein regions. In this work we use two different Young's modulus E for the radial artery and cephalic vein to account for their different elastic properties. Since the study focuses on the first days after surgery, before the onset of tissue remodeling, the artery is set to
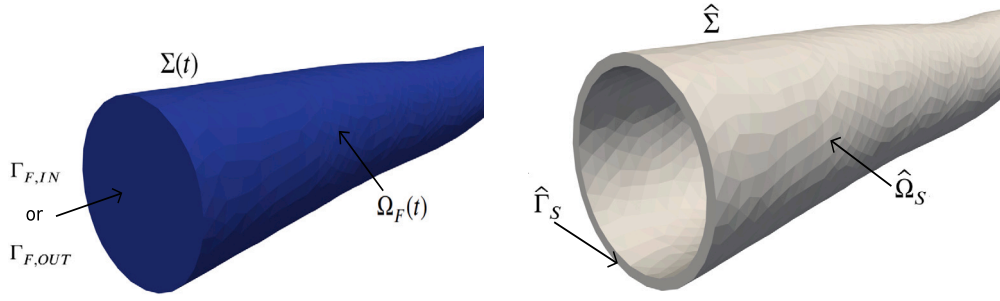
Fig. 3. Left: Fluid domain. Right: Structure domain.

be stiffer than the vein; moreover, we also geometrically differentiate the vein and the artery by accounting for their different wall thicknesses τ. The value of the Poisson's coefficient ν is equal for both the vessels.

3. Mathematical models and numerical methods

3.1. The fluid-structure interaction problem

The fluid dynamics is modeled using the incompressible homogeneous Navier-Stokes equations written in the arbitrary Lagrangian-Eulerian (ALE) formulation, assuming a laminar regime. The dynamics of the vessel wall is modeled through the linear elasticity equations written in a Lagrangian framework. This is justified since AVFs experience small vessel wall displacements with respect to their reference configuration [49,21]. For the sake of notation, from now on, the quantities written in a pure Lagrangian framework (reference configuration) are marked with $\hat{\cdot}$. In this respect, we introduce a fluid mesh motion $\mathbf{d}_F$, solution of a harmonic extension within the lumen of the boundary displacement. This allows us to move the fluid mesh as follows

$$\mathbf{x}(t) = \hat{\mathbf{x}} + \hat{\mathbf{d}}_F(\hat{\mathbf{x}}, t) \qquad \forall \hat{\mathbf{x}} \in \hat{\Omega}_F .$$

Referring to Fig. 3, let $\Omega_F(t)$ and $\hat{\Omega}_S$ be the fluid and structure domains, respectively, and $\Sigma(t)$ the interface between the fluid and the structure domains. Let $\mathbf{u}(\mathbf{x}, t) : \Omega_F(t) \to \mathbb{R}^3$ the fluid velocity, $p(\mathbf{x}, t) : \Omega_F(t) \to \mathbb{R}$ the fluid pressure, $\hat{\mathbf{d}}(\mathbf{x}, t) : \hat{\Omega}_S \to \mathbb{R}^3$ the displacement of the vessel walls, and $\mathbf{u}_F$ the velocity of the fluid mesh. In the following, we report the formulation of the FSI problem:

For any $t > 0$, find $\mathbf{u}$, p, $\hat{\mathbf{d}}$, such that:

$$\rho_F \frac{\partial \mathbf{u}}{\partial t} + \rho_F((\mathbf{u} - \mathbf{u}_F) \cdot \nabla)\mathbf{u} - \nabla \cdot T_F(\mathbf{u}, p) = \mathbf{0} \qquad \text{in} \quad \Omega_F(t), \tag{1a}$$

$$\nabla \cdot \mathbf{u} = 0 \qquad \text{in} \quad \Omega_F(t), \tag{1b}$$

$$\mathbf{u} = \frac{\partial \mathbf{d}}{\partial \mathbf{t}} \qquad \text{on} \quad \Sigma(t), \tag{1c}$$

$$T_F(\mathbf{u}, p)\mathbf{n} = T_S(\mathbf{d})\mathbf{n} \qquad \text{on} \quad \Sigma(t), \tag{1d}$$

$$\rho_S \frac{\partial^2 \hat{\mathbf{d}}}{\partial t^2} - \nabla \cdot \hat{T}_S(\hat{\mathbf{d}}) = \mathbf{0} \qquad \text{on} \quad \hat{\Omega}_S, \tag{1e}$$

$$-\Delta \hat{\mathbf{d}_F} = \mathbf{0} \qquad \text{on} \quad \hat{\Omega}_F, \tag{1f}$$

$$\hat{\mathbf{d}}_F = \hat{\mathbf{d}} \qquad \text{on} \quad \hat{\Sigma}, \tag{1g}$$

with suitable initial conditions on $\mathbf{u}$, $\hat{\mathbf{d}}$, $\dot{\hat{\mathbf{d}}}$ and where ρ_F and ρ_S are the fluid and structure densities. Equations (1c) and (1d) represent the interface conditions stating the continuity of fluid and structure velocities and forces. Problem (1) needs to be equipped with suitable boundary conditions which will be detailed in the next section. Notice that $\mathbf{u}_F = \dot{\mathbf{d}}_F$, $T_F(\mathbf{u}, p) = -pI + \mu_F(\nabla \mathbf{u} + \nabla \mathbf{u}^T)$ is the fluid Cauchy stress tensor with μ_F the fluid dynamic viscosity and $\hat{T}_S(\hat{\mathbf{d}}) = \lambda \nabla \cdot \hat{\mathbf{d}} I + \mu_S(\nabla \hat{\mathbf{d}} + \nabla \hat{\mathbf{d}}^T)$ is the structure Piola-Kirchhoff stress tensor. It is worth noting that $\lambda = \frac{E\nu}{(1+\nu)(1-2\nu)}$ and $\mu_S = \frac{E}{2(1+\nu)}$ are the Lamé constants, where ν is the Poisson's coefficient.

The time discretization is obtained using a second order backward differentiation formula [36] (BDF2), for both fluid and structure problems [53]. The FSI system is linearized owing to the inexact Newton method, in particular neglecting shape derivatives in the Jacobian matrix. The problem is solved monolithically by using a block preconditioner based on the SIMPLE preconditioner for the fluid subproblem [25] and using the GMRES method with an absolute tolerance of 10^{-10}. The geometry problem (see (1f) and (1g)) is treated implicitly, i.e. at every Newton subiteration the fluid mesh is moved accordingly to the harmonic motion.

The space discretization of the Navier-Stokes equations is obtained using piecewise linear Finite Elements ($\mathbb{P}1 - \mathbb{P}1$) for both the velocity and pressure, stabilized by means of the SUPG-PSPG method [69], which allows also to control the advection dominated regime. The elasto-dynamics problem is discretized using $\mathbb{P}1$ Finite Elements.

Concerning the parameters for the fluid problem, the density and the dynamic viscosity of the blood are $\rho_F = 1.060 \, g/cm^3$ and $\mu_F = 0.035 \, g/(cm \cdot s)$. While for the elastic properties, we set the artery stiffer than the vein, i.e. $E_A = 2.5$ MPa (suitable literature range 2.68 ± 1.68 MPa) [45] and $E_V = 0.5$ MPa (suitable literature range 0.45 ± 0.05 MPa) [60], respectively; moreover, we impose the same Poisson's coefficient $\nu_V = \nu_A = 0.45$ [6,67] and an elastic surrounding tissue coefficient $\alpha_R = 2.5 \times 10^6 \, \frac{Pa}{cm}$ (see Eq. (2)) for both the radial artery and the cephalic vein. Such values have been properly calibrated to obtain physiological displacements coherent to the literature. The cephalic vein and the radial artery are assumed to have the same density $\rho_S = 1.2 \, g/cm^3$ [41]; we also assume that the two patients have the same mechanical properties. Notice that for the arterial and venous compliance we use literature values. Alternatively, there are two main techniques used to measure the mechanical properties of a vessel. In [70], the plethysmography, a technique to measure the venous distensibility, is described in the context of the arteriovenous fistula; while, in [20], a technique based on ultrasound is explained with its protocol and, it is also compared to the plethysmography finding a good correlation.

The numerical results are obtained using the LifeV [24–26,35] Finite Element library for the approximation of Partial Differential Equations by the Finite Elements Method. The software has been developed at École Polytechnique Fédérale de Lausanne, MOX laboratory at Politecnico di Milano, INRIA-Paris, and Emory University [10]. The numerical simulations were run at MOX laboratory clusters on 4 processors Xeon E5-4610 having a total of 56 cores and RAM of 504 GB. To numerically solve the FSI problem, we introduce a uniform time discretization in which Δt is the step size and T is the heartbeat period. In all the numerical experiments, we set $\Delta t = 10^{-3} s$ and $T = 0.8s$. It is worth pointing out that we consider a null initial condition and we perform some heartbeat cycles until the results are at regime. Specifically, we found that the results of the second and third heartbeat cycles are very similar, so in what follows we consider the results of the second heartbeat.

3.2. Boundary conditions

Fluid outlet boundary conditions are imposed by means of an absorbing resistance R_a [53]:
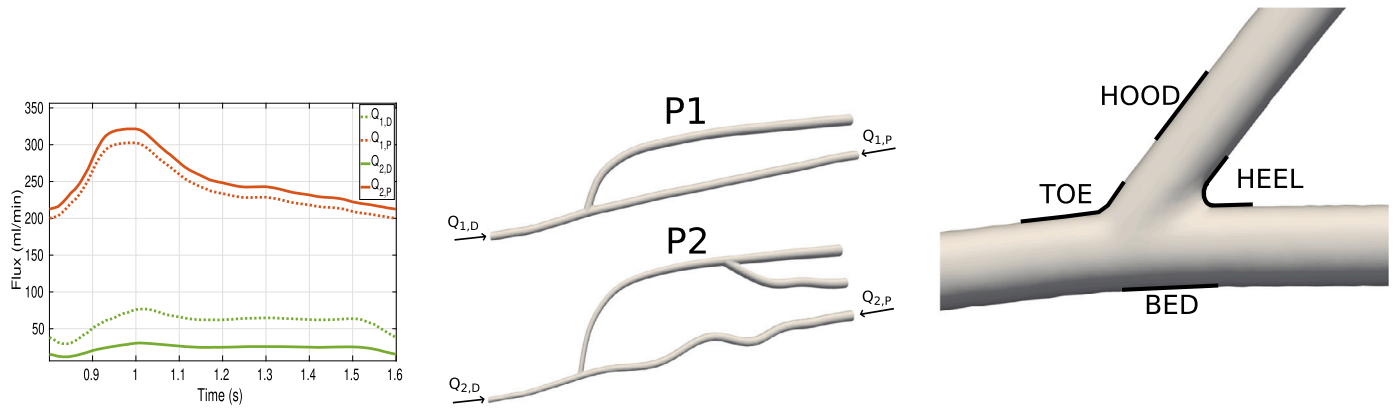
Fig. 4. Prescribed inlet flow rates (left), computational domains (middle), zones of clinical relevance at the anastomosis region (right) [71].

$$R_a = \sqrt{\frac{\rho_f \beta}{2}} \frac{1}{A_F^{\frac{3}{4}}}, \quad \beta = \frac{E\tau\pi}{(1-\nu^2)A_F}, \quad \tau = \sqrt{\frac{A_F + A_S}{\pi}} - \sqrt{\frac{A_F}{\pi}},$$

where A_F is the area of the fluid outlet boundary and A_S is the area of the outlet surface of the structure. Therefore, assuming a constant normal traction on $\Gamma_{F,OUT}$, the outlet fluid condition is defined as

$$T_F(\mathbf{u}, p)\mathbf{n} \cdot \mathbf{n} = R_a \int_{\Gamma_{F,OUT}} \mathbf{u} \cdot \mathbf{n} \, d\gamma + P_{EXT} \quad \text{on} \quad \Gamma_{F,OUT},$$

where $P_{EXT} = 75$ mmHg is the diastolic systemic pressure and with homogeneous tangential traction conditions [34].

Regarding both the proximal and distal inlets, we enforce a Dirichlet condition by considering a parabolic velocity profile:

$$\mathbf{u}(\mathbf{x}, t) = -\frac{Q_{IN}}{A_F \rho_F}\left(1 - \frac{r^2}{R^2}\right)\mathbf{n} \quad \text{on} \quad \Gamma_{F,IN},$$

where Q_{IN} is the prescribed flow rate taken from [68], plotted in Fig. 4. The values are those typical of a non-mature fistula and in agreement with the literature [13]. Notice that we consider here unsteady and pulsatile inlet conditions. This is of crucial importance in order to obtain physiological results. Using a steady fluid dynamics model would nullify the reliability of the numerical results, especially for the velocity field, i.e., vorticity creation and transition to turbulence.

Concerning the structure problem, since both the inlet and outlet boundaries are far enough from the zone of hemodynamic interest, i.e. the anastomosis region, the boundary conditions for the vessel displacement are imposed through a zero-displacement constrain on both the axial and radial directions:

$$\hat{\mathbf{d}} = \mathbf{0} \quad \text{on} \quad \hat{\Gamma}_S.$$

Moreover, to reliably simulate the displacement of the vessels, we model the presence of the surrounding tissue around the vein and the artery by means of the following Robin condition on the external surface $\hat{\Gamma}_{EXT}$ [58]:

$$\alpha_R \hat{\mathbf{d}} + \hat{T}_S(\hat{\mathbf{d}})\mathbf{n} = P_{EXT} \quad \text{on} \quad \hat{\Gamma}_{EXT}, \tag{2}$$

where α_R is the elastic coefficient of the surrounding tissue and we assumed that the surrounding tissue pressure is again equal to the diastolic one.

4. Results & discussion

In this section, we report the obtained numerical results on the parametric configurations of the two end-to-side RCAVF-SS patients. The results are showed through the following outline. In Sec. 4.1, we describe the hemodynamics and structure quantities of interest. In Sec. 4.2, we discuss the numerical results concerning the hemodynamic quantities,

whereas in Sec. 4.3 the outcomes related to the structure quantities. Finally, in Sec. 4.4 and Sec. 4.5, we summarize our outcomes and the limitations of this work.

4.1. Relevant hemodynamic quantities

Concerning the hemodynamics, we are interested in the following quantities:

- The velocity and pressure distribution at the anastomosis region. Indeed, disturbed flow, abnormal recirculation regions and elevated pressure may provoke conditions favoring intimal hyperplasia (IH) [40];
- The Wall Shear Stress (WSS). It is the magnitude of a vector quantity representing the tangential shear stress caused by the fluid flowing on the vessel wall:

$$WSS = \sigma_F \mathbf{n} - (\sigma_F \mathbf{n} \cdot \mathbf{n})\mathbf{n}.$$

In the systemic arterial context, a normal WSS is considered between $1-7$ Pa [28]. In particular, small (< 1 Pa) and oscillatory values are strictly connected to cardiovascular complications such as IH and stenosis. On the other hand, high WSS (> 7 Pa) protects against IH, but it may provoke endothelial cell cleavage and induce thrombosis [28]. As stated in [15], the constant presence of high WSS may result in VA dysfunction;

- The Oscillatory Shear Index (OSI). It is a scalar quantity representing the degree of shear reversal in a pulsatile flow; it goes from 0 in a uni-directional flow to 0.5 in a reversing flow with no mean shear direction [4]; elevated values of OSI, that is high oscillatory WSS, favor the conditions that could lead to stenosis triggering venous IH [63,28,29,17]. Let us define T as the final time of the simulation, the OSI is defined as follows:

$$OSI(\mathbf{x}) = \frac{1}{2}\left[1 - \frac{||\int_0^T \mathbf{WSS}(t, \mathbf{x}) \, dt||}{\int_0^T ||\mathbf{WSS}(t, \mathbf{x})|| \, dt}\right];$$

- Time Averaged Wall Shear Stress (TAWSS). It is a scalar quantity measuring the time-average shear. Fixed a space location, the TAWSS is defined as:

$$TAWSS(\mathbf{x}) = \frac{1}{T}\int_0^T ||\mathbf{WSS}(t, \mathbf{x})|| \, dt.$$

Small TAWSS values could bring to IH formation and stenosis [17]. In [13], the authors find that regions with high OSI are associated with low TAWSS in the AVF context.

Concerning the vessel dynamics, we are interested in the following variables:
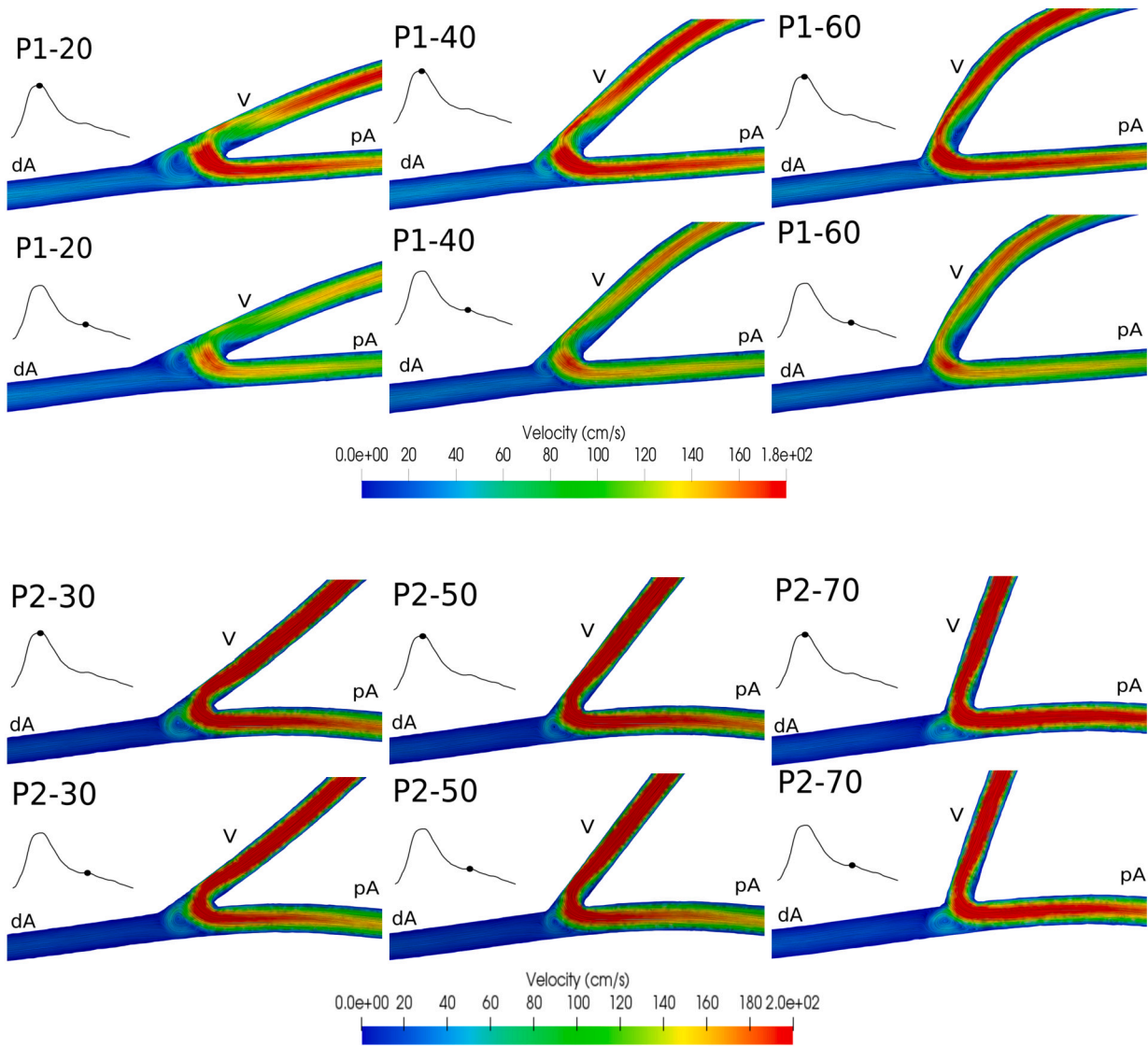
Fig. 5. Velocity field at the anastomosis region. First Row: P1 at the systolic peak ($t = 1s$) is reported. Second Row: P1 at the deceleration phase ($t = 1.3s$) is reported. Third Row: P2 at the systolic peak ($t = 1s$) is reported. Fourth Row: P2 at the deceleration phase ($t = 1.3s$) is reported. pA = proximal artery, dA = distal artery, V = vein. Notice the different scales used for the two patients, to highlight differences among anastomosis angles.

- Displacement of the vessel walls. Since the vessel dilation is necessary to obtain the requested flow rate by the dialyzer [42], we aim to understand which is the role of the vessel displacement in the context of fistula maturation. In particular, since there is no information in the literature, we want to establish which is the correlation between the displacement of the cephalic vein with the maturation failure of the juxta-anastomotic region. It is worth noting that we compute the displacement w.r.t the reference condition;

- Von Mises stress. It is one of the most used criteria for checking yield conditions [1,64]. We are interested in computing which parts of the vessel walls are subjected to a large mechanical stress, to understand if a correlation between the high-stress zones and VA failure can be stated. Considering σ as the Cauchy stress tensor corresponding to T_S, the Von Mises stress is defined as follows:

$$\sigma_v = \frac{1}{2}\left[(\sigma_{11}^2 - \sigma_{22}^2) + (\sigma_{22}^2 - \sigma_{33}^2) + (\sigma_{33}^2 - \sigma_{11}^2) + (\sigma_{12}^2 - \sigma_{13}^2) + (\sigma_{23}^2)\right].$$

For the analysis of these quantities, we often refer to specific regions of the fistula of clinical relevance, since they are considered crucial for the study of stenosis due to IH, see Fig. 4, right.

4.2. Blood dynamics analysis

In this section, we aim to analyze the numerical results concerning fluid dynamics. For all the results, the temporal instants (systolic peak and deceleration phase) refer to the proximal inlet flow rate waveform (see Fig. 4). We found a systolic Reynolds number of about 2000 and a Womersley number equal to 4.7.

In Fig. 5, we report the velocity field on a longitudinal slide at two representative instants (systolic peak $t = 1.0$ and deceleration phase $t = 1.3$ s), for P1 and P2. Regarding P1, we notice the creation of a huge vortex at the toe (left part of the anastomosis) and a little vortex at the heel (right-upper part of the anastomosis). Coherently, passing from the systolic peak to the deceleration phase, the magnitude and the dimension of the main vortex decrease; the deceleration of the flow does not cause any further abnormal recirculation region and for the entire cardiac cycle the toe of the anastomosis is subjected to the action of the vortex. We believe that since the AVF is far from the heart, and since the presence of an arteriovenous shunt causes a radical drop in peripheral resistance, it is less affected by the passage towards the different phases of the cardiac cycle, and there is no vortex dissipation at the anastomosis region. The intensity and the shape of the vortex change
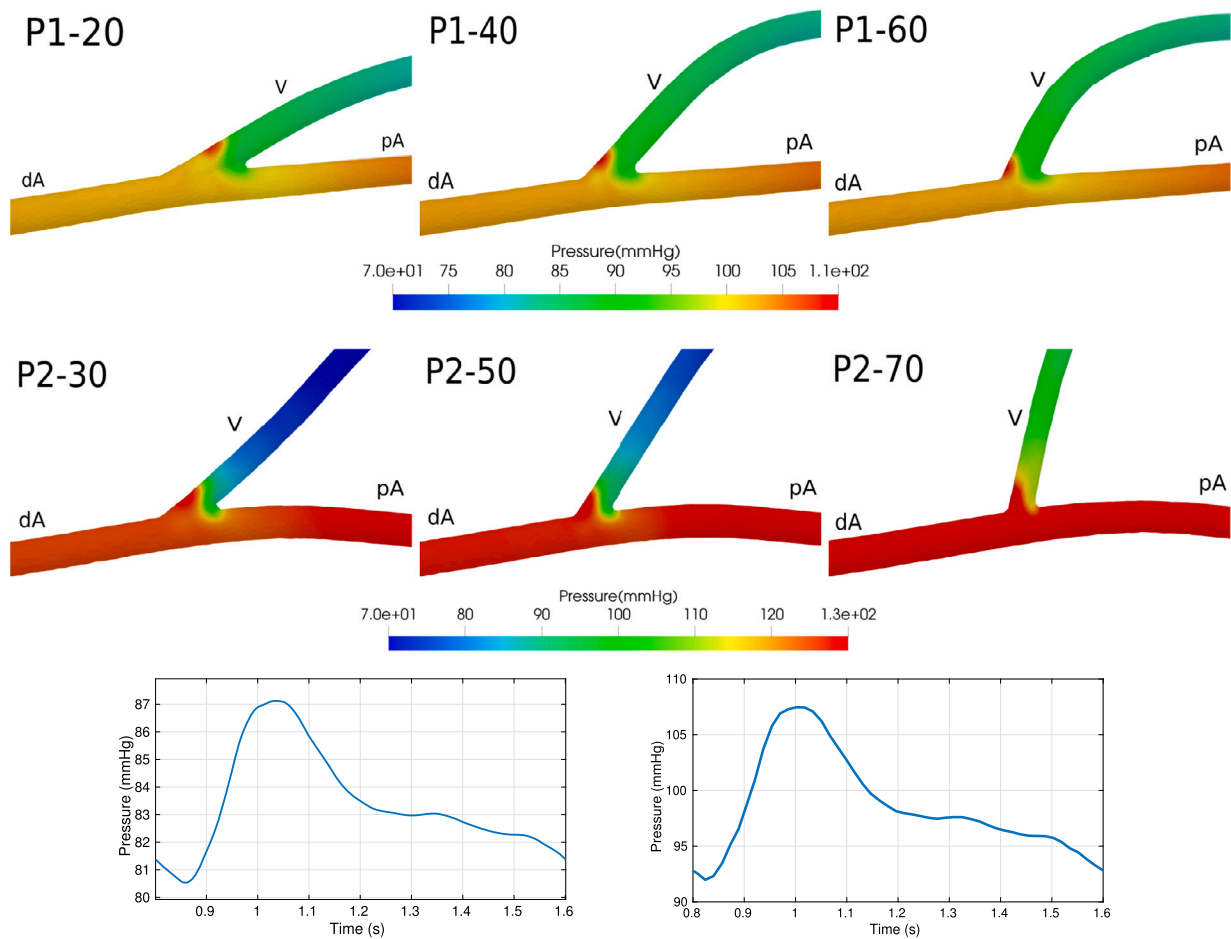
Fig. 6. Top: Pressure field at the anastomosis region. First row: P1 configurations at the systolic peak ($t = 1s$). Second row: P2 configurations at the systolic peak ($t = 1s$). pA = proximal artery, dA = distal artery, V = vein. Notice the different scales used for the two patients, to highlight differences among anastomosis angles. Bottom-left: Computed pressure at the vein outlet in the case of P1-20. Bottom-right: Computed pressure at the distal inlet in the case of P1-20.

Table 2
Diameter of the cephalic vein (D_c) and radial artery (D_r) for P1 and P2.

	P1	P2
D_r	2.85 mm	2.28 mm
D_c	3.03 mm	2.05 mm
$\frac{\lvert (D_c - D_r) \rvert}{D_r} * 100$	6.3%	11.2%

by varying the anastomosis angle; in particular, we notice that P1-20 appears to be the configuration that induces more disturbed flow; on the other hand, P1-60 is the most protective configuration leading to a less chaotic condition. Regarding P2, we do not see relevant differences in the vortex dimension and velocity magnitude between the two different instants of the cardiac cycle. Moreover, differently from P1, there are no changes in the blood dynamics pattern when varying the anastomosis angle; the vortex at the center of the anastomosis of P2 does not decrease its dimension when the anastomosis angle increases. We believe this is due to the fact that the diameter of the cephalic vein is too small in comparison to the radial artery. In Table 2, we report the diameters of the cephalic vein and radial artery of P1 and P2 to highlight the correlation with the disturbed flow.

In [43], the authors state that a cephalic vein diameter below 2 mm and a diameter of the radial artery below 1.5 mm could play a crucial role in fistula failure. In [8] and [73], the authors find that to favor fistula maturation, the diameter of the cephalic vein should be at least of 2.5 mm. This is confirmed by our results since with P2 (diameter of the cephalic vein smaller than 2.5 mm) we observe the presence of a vortex

that leads to a disturbed flow independently of the anastomosis angle. Conversely, in P1 (diameter of the cephalic vein larger than 2.5 mm), if the anastomosis angle is large enough the vortex disappears and the flow becomes more regular. Therefore, we suggest that both the anastomosis angle and the diameter of the vessels could play a fundamental role in avoiding the generation of disturbed flow and thus in fistula maturation. Notice that the values of the velocity magnitude are coherent with other works [27,18] and with experimental measures [32].

In Fig. 6, bottom, we report the computed outlet and distal inlet pressures for P1-20 as representative case. Notice that we found physiological range in accordance to the pressure drops reported in [23]. In Fig. 6, top and middle, we describe the pressure field of the anastomosis region at the systolic peak ($t = 1.0$) for P1 and P2. Here, we also observe that for both patients, the highest value of the pressure is registered between the toe and the hood. This is coherent with the velocity field, since at these locations there is a stagnation point due to the high flow rate coming from the proximal radial artery which goes perpendicular to the cephalic vein walls. The pressure field along the anastomosis region has the same pattern in all six configurations, but with different magnitudes. It is known that in healthy patients, the cephalic vein has pressures of about 7-15 mmHg [54]; since in the AVF the cephalic vein is connected with the systemic arterial network, coherently its pressure increases suddenly. In P1, where the diameter of the vessels is similar and, in particular, the cephalic vein diameter is larger than the radial artery diameter (see Table 2), the pressure inside the cephalic vein is almost equal in all three configurations, reaching a value of blood pressure close to that of the systemic arterial circulation. In P2, we believe that the small diameter of the cephalic vein causes a low pressure along
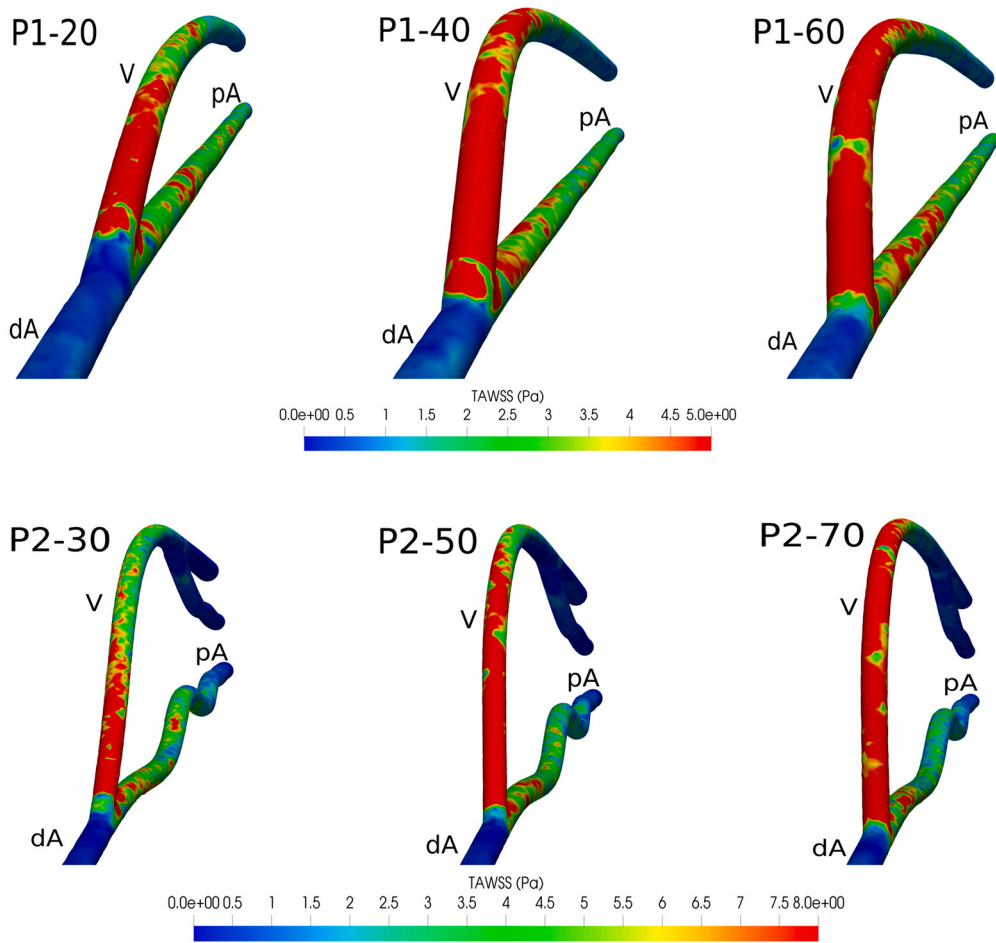
Fig. 7. First Row: TAWSS of P1. Second Row: TAWSS of P2. pA = proximal artery, dA = distal artery, V = vein. Notice the different scales used for the two patients, to highlight differences among anastomosis angles.
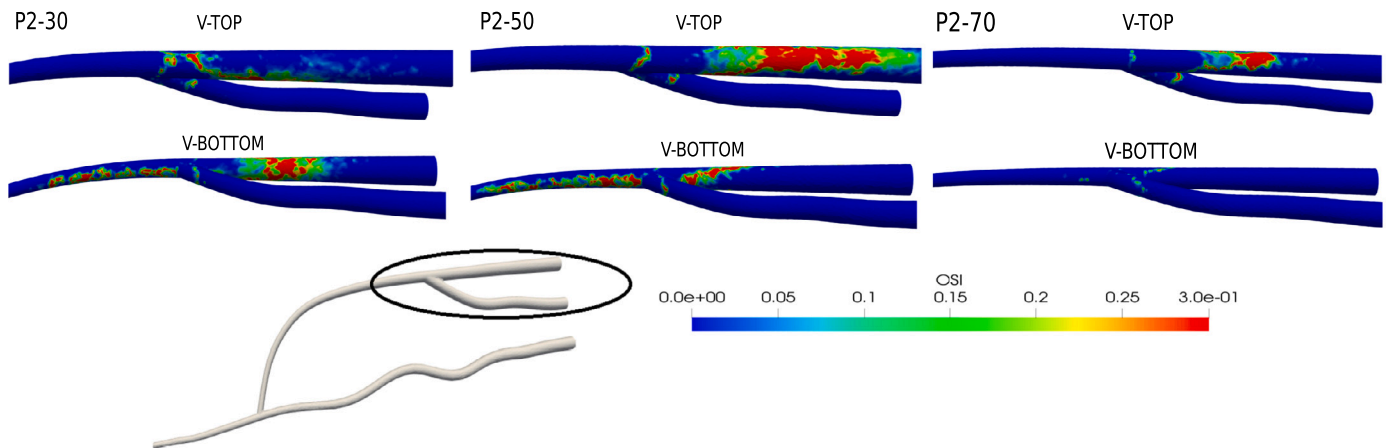

Fig. 8. P2. OSI at the distal part of the vein, represented in the circle. V-TOP = vein top view. V-BOTTOM = vein bottom view.

the cephalic vein (and as a consequence an increase of the velocity field, see Fig. 5) making the dilation of the cephalic vein more difficult.

In Fig. 7, in the first and second rows, we report the TAWSS for P1 and P2, respectively; while, in Fig. 8, we evaluate the OSI, reporting the top and bottom view of the cephalic vein for P2.

Regarding the TAWSS, for all the configurations, we note that the distal part of both the radial artery and cephalic vein is less subjected to the action of shear stress making them susceptible zones for the creation of IH and stenosis. The values and the regions of high and low

TAWSS are in agreement with [18]. The variation of the anastomosis angle and the cephalic vein diameter do not seem to have any effect on the WSS at the distal part of the radial artery, while an increase of the anastomosis angle causes an increase of the TAWSS at the proximal and distal part of the cephalic vein. In the clinical literature, it is well known that the juxta-anastomotic region (i.e. the proximal part of the cephalic vein) is at high risk for stenosis [59], therefore since the increase of the anastomosis angle causes an increase of the TAWSS in the proximal part of the cephalic vein, we believe that P1-60 and P2-70 are the best
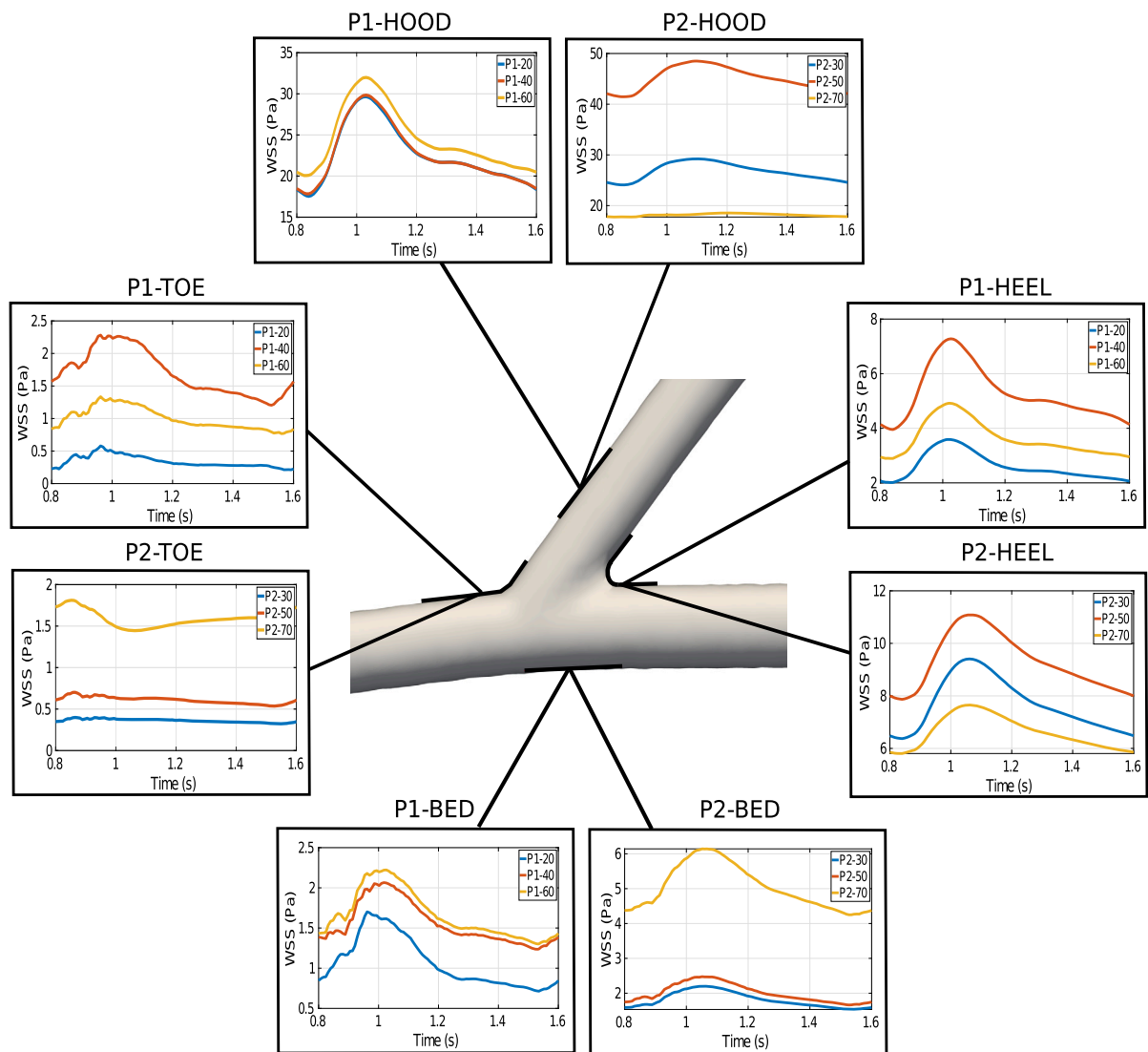
Fig. 9. P1 & P2. Space-averaged WSS at the heel, bed, hood and toe of the anastomosis. Notice the different scales in the figures, to highlight significant differences among the anastomosis angles.

configurations for the protection from stenosis, independently from the cephalic vein diameter. In P2, the small diameter of the cephalic vein causes a decrease of pressure along the cephalic vein (see Fig. 6), but on the other hand it generates an increase of the velocity field, i.e. an increase of the TAWSS (which should be better to avoid the stenosis).

In Fig. 8, the OSI is analyzed with particular focus on the distal part of the cephalic vein of P2. The bifurcation at the distal part of the cephalic vein generates an anomalous pattern of the OSI in both the top and bottom part of the vein. P2-30 and P2-50 seem to be the worst scenario generating an extremely high oscillatory shear stress. P2-70 is more protective, especially in the bottom part of the cephalic vein. The only parameter changing between the three configurations of P2 is the anastomosis angle, suggesting a strong correlation between generation of stenosis in the distal segment of the cephalic vein and the anastomosis angle. In accordance with [30], the distal part of the cephalic vein is one of the most affected sites of stenosis; here, we coherently detect low value of WSS and high OSI. As stated in [66], after and before bifurcations or branches, regions of flow disturbance and flow separation are created, in which the OSI can increase, creating favorable conditions for development of stenosis in the distal segment of the cephalic vein. We do not report OSI values for P1 since we encounter a quasi-zero value along all the arteriovenous fistula except at the toe of the anastomosis

of P1-20, but we consider those values extremely low and not of clinical relevance. We point out that our FSI results show a completely different OSI pattern compared to the rigid study [68], where the largest OSI values are found near the anastomosis region, whereas in this case the distal part of the vein is affected by the highest OSI values.

In Fig. 9, we report the space-averaged WSS at specific regions in the toe, hood, heel and bed of the anastomosis for P1 and P2 at every instant of the cardiac cycle. Except for P2-HOOD and P2-HEEL, we observe that the configurations with the lowest angles (P1-20 and P2-30) generate the lowest WSS. Regarding the toe, both P1 and P2 experience very low shear stress, in particular, the conditions which seem to better protect the toe of the anastomosis are those represented by the angles P1-40 and P2-70, but in general, all six configurations are characterized by low WSS. Here, we note that WSS has an oscillate-in-time behavior until the systolic peak, in particular, P1 has the highest oscillations. Looking at the bed, we see that P2 again is characterized by higher WSS values and P1 has a relevant oscillating-in-time behavior before the systolic peak. Also for the bed of the anastomosis, the low angle configurations (P1-20,P1-40,P2-30,P2-50) show lower value of shear stress, while P1-60 and in particular P2-70 have normal values guaranteeing a better protection against IH. It is worth noting that the bed of the anastomosis is another typical site for the creation of the stenosis [66]. Considering
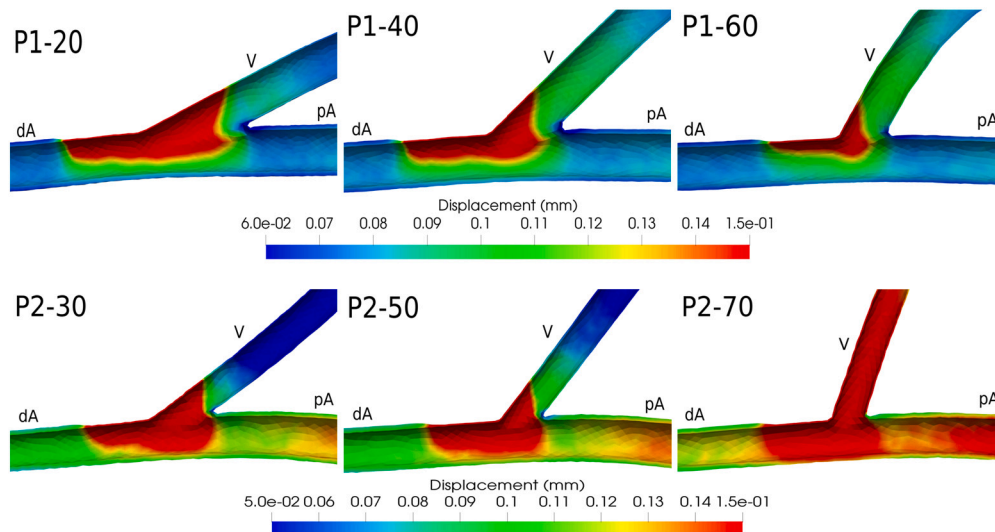
Fig. 10. Displacement field at the anastomosis region. First row: P1 configurations at the systolic peak ($t = 1s$). Second row: P2 configurations at the systolic peak ($t = 1s$). Notice the different scales in the figures, to highlight significant differences among the anastomosis angles. pA = proximal artery, dA = distal artery, V = vein.

that in AVF context, an accepted threshold for a normal WSS is 7 Pa [28], at the heel of the anastomosis we encounter values close to this limit. In particular concerning P1, P1-40 at the systolic peak reaches the threshold, while P1-20 and P1-60 feature values largely lower than it. Referring to P2, P2-70 seems the best configuration while P2-30 and P2-50 exceed the WSS limit practically in all the phases of the cardiac cycle. Finally, we look at the hood of the anastomosis which can be considered part of the juxta-anastomotic region. Here, the values of the WSS are extremely high for all the configurations. Looking at P1, the anastomosis angle has a very small effect on the values of WSS, while in P2 the best condition is P2-70 which is able to maintain the value of WSS at the lowest level possible, but above the physiological threshold. In general, P2 has higher values of WSS in all regions, we believe that this condition is due to higher velocities obtained.

4.3. Structural analysis results

In this section, we present the numerical results concerning the vessel wall structural quantities.

Referring to the displacement field, in Fig. 10 we report, by means of a longitudinal slice, the displacement magnitude of the anastomosis region at the systolic peak ($t = 1s$) for P1 and P2. In particular, we observe two opposite trends for P1 and P2. In the former, an increase of the anastomosis angle generates a decrease of the displacement magnitude at the anastomosis region (between the toe and the floor) and a light increase of the displacement along the juxta-anastomotic region. Instead, in P2 we observe that the increase of the anastomosis angle provokes a strong increase of the displacement in both the anastomosis and juxta-anastomotic regions. In general, since the cephalic vein has a larger compliance, we expect higher displacements, but this is not the case. The reason is that the systemic venous system works with lower pressure (see Fig. 6) and thus the cephalic vein is not forced to expansion. Focusing on P2, we believe that the small diameter of the cephalic vein generates an increase in the velocity field and a decrease of the pressure; therefore, the decrease of the latter causes the diminishing of the displacements (see P2-30 and P2-50). Moreover, since the small diameter of the cephalic vein increases the difficulty of the blood to flow into it, coherently the flow stagnates in the bottom part of the anastomosis region, generating an increase of the displacement, also in the floor of the anastomosis; this is particularly relevant in P2-70. This is in accordance with the results found in [72]. For both P1 and P2, starting from the distal artery, the region of high displacements begins at the

toe of the anastomosis where there is a sudden change in the thickness; on the other part, close to the heel, we do not observe any important variation in the displacement. These values of displacement magnitude are in agreement with the numerical simulations reported in [49].

Considering the Von Mises stress, in Fig. 11, we evaluate the space-averaged Von Mises stress at heel, bed, hood and toe of the anastomosis for P1 and P2, respectively. We observe that the P2 configurations display twice the mechanical stress observed in P1 in all parts of the anastomosis region. Since this behavior is consistent for all the configurations and parts of the anastomosis region, we think that this increase is due to the small diameter of the cephalic vein. In the case of P1, where the cephalic vein is larger than the radial artery, we note that there are very few differences between P1-40 and P1-60; on the other hand, considering P2, P2-70 seems the worst possible configuration generating high stress in all the regions. From a mechanical point of view, when the cephalic vein is larger than the radial artery (P1), an increase in the anastomosis angle is not able to modify the stress at the anastomosis region. Conversely, for small angles of P2, the stress distribution is not significantly affected by the change of the angle, but it increases a lot with P2-70. Coherently, the high displacement zones are associated with a high value of Von Mises stress as previously seen in other studies [9,65].

4.4. Final discussion

In this work, the principal aim was to investigate the blood/vessel dynamics in an arteriovenous fistula during the first days after the creation of the anastomosis. Specifically, we are not interested in studying the fluid dynamics when the fistula has matured i.e. when the remodelling of the cephalic vein is completed.

We stress that our 3D geometry models did not account for individual variations, since we virtually built the different angle configurations starting from the same geometry. Since the main aim of this study was to isolate the influence of the anastomosis angle on the hemodynamics, we decided to consider the same geometries for both artery and vein, where only the anastomosis angle was varied, in order to "isolate" the hemodynamic changes due to the angle change solely.

Our results show that both the diameter of the cephalic vein and the anastomosis angle play a fundamental role in the generation of recirculation regions, abnormal values of WSS, OSI and mechanical stress. For clarity, we group our cases in four scenarios:
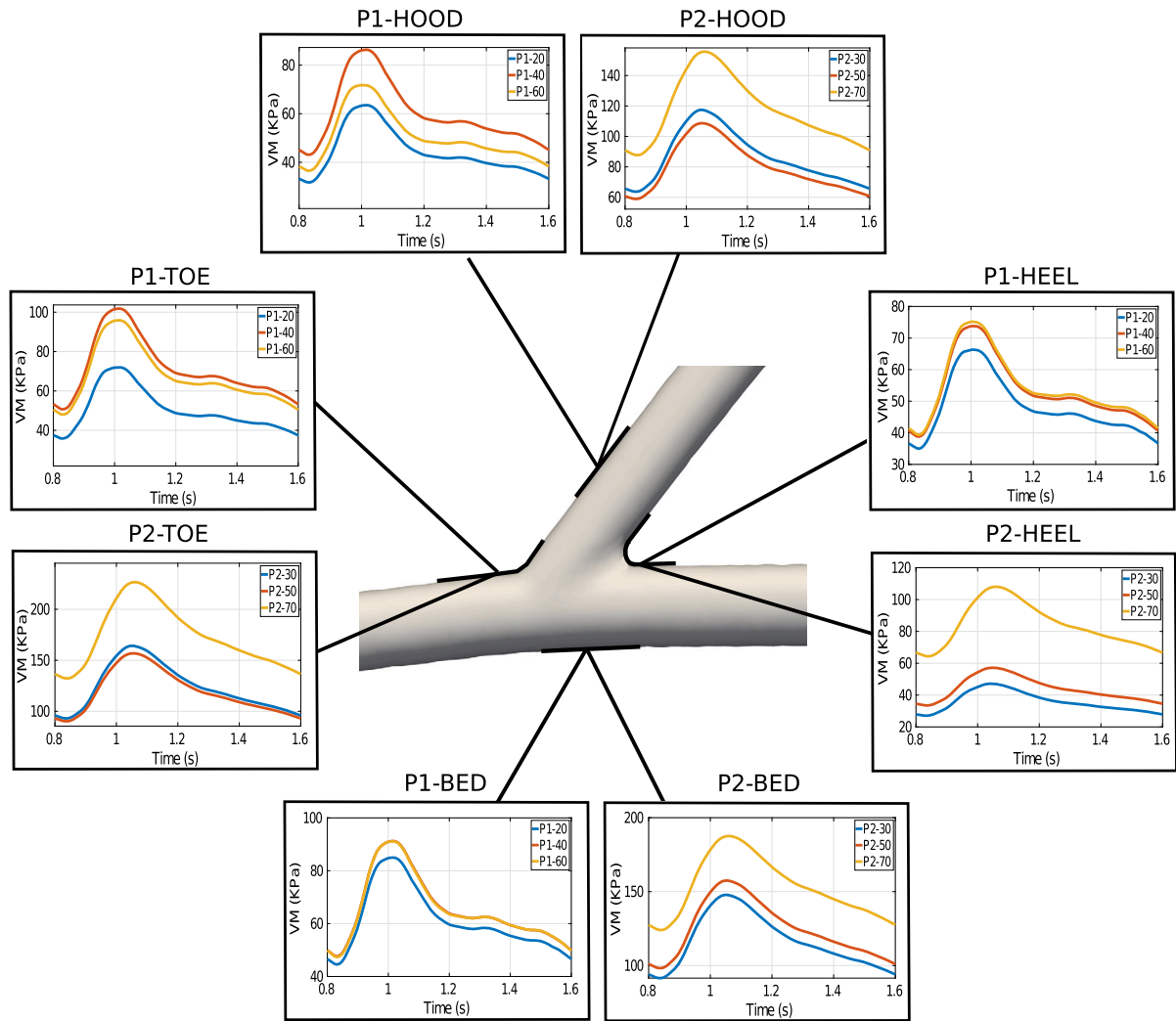
Fig. 11. P1 & P2. Space-averaged Von-Mises stress at the heel, bed, hood and toe of the anastomosis. Notice the different scales in the figures, to highlight significant differences among the anastomosis angles.

a) Low anastomosis angle and large diameter of the cephalic vein (P1-20, P1-40)
b) High anastomosis angle and large diameter of the cephalic vein (P1-60)
c) Low anastomosis angle and small diameter of the cephalic vein (P2-30, P2-50)
d) High anastomosis angle and small diameter of the cephalic vein (P2-70)

When the cephalic vein has a small diameter compared to that of the radial artery (P2, case c and d above, see Table 2), we find:

• Strong increase of the velocity. Generally, high velocity means high WSS which protects against IH, but when the diameter of the cephalic vein is too small as in this case, the velocity is excessively high and the WSS takes on abnormal values. This condition could favor the generation of thrombosis;
• The big vortex at the anastomosis region is presented for all the configurations with the same shape and intensity, the anastomosis angle does not have any effect on the blood dynamics;
• Low pressure. The blood does not favor the dilation of the cephalic vein. This condition is unfavorable to fistula maturation;
• High Von Mises stresses (larger than P1) in all the parts of the anastomosis region.

When the cephalic vein has a larger diameter than the radial artery (P1, case a and b above), the variation of the anastomosis angle influences both the blood dynamics and mechanics of the vessels:

• Case a (P1-20, P1-40):
  – Blood dynamics: Constant presence of a big vortex at the anastomosis region, physiological value of the pressure and unhealthy value of the WSS (too low);
  – Vessel dynamics: The displacements are larger and the mechanical stress lower than Case b in all the parts of the anastomosis region (especially for P1-20).
• Case b (P1-60):
  – Blood dynamics: The presence of the vortex at the anastomosis region is almost absent, physiological values of pressure and WSS are found;
  – Vessel dynamics: Lower displacements and higher mechanical stresses than Case a (especially with respect to P1-20).

When the diameter of the cephalic vein is large enough, we confirm that the variation of the anastomosis angles can have a strong effect on the blood dynamics and vessel wall dynamics. In particular, as stated in [68], we confirm that high anastomosis angles (P1-60) are the best in avoiding the recirculation zone and maintaining a healthy WSS. We cannot state the same for P2-70, since we think that the small diameter

of the cephalic vein has more influence on the blood dynamics than the change of the anastomosis angle.

It is worth noting that the bifurcation at the distal vein (see Fig. 8) is a zone prone to the generation of high values of OSI; in particular, the highest anastomosis angle (P2-70) is the best one in the reduction of OSI.

Finally, we notice that for P1 we found somehow opposite conclusions than [27] in terms of best anastomosis angles to reduce the disturbed flow, since the authors of that study found that the smallest angle should protect from disturbed flow. This could be due to the differences of the two models: FSI (ours) vs CFD ([27]), different compliance for artery and vein in our case, different dimensions of artery and vein thicknesses in our case, real vs ideal geometries, complete geometry including a distal branch in our case.

To conclude, we would like to emphasize possible clinical implications of our findings. While fashioning the fistula anastomosis, the angle may be influenced by some surgical choices that can be made by the surgeon in order to yield larger or smaller angles. Primarily, the length of the vein swing-segment (the segment of vein that is surgically prepared and mobilized to be approached to the artery), may be chosen to be longer to bring the vein more parallel to the artery, yielding smaller angles, or may be left shorter in order to determine a larger angle of the anastomosis. Long swing segments are also known to be prone to develop intimal hyperplasia due to excess manipulation and wall devascularization. Further techniques include the use of side branches (venous branch-patch) or the vein-mouth technique, to allow for large angle anastomoses. The smooth loop technique also allows to radically modify the angle of incidence of the vein upon the artery, although this normally requires the preparation of a relatively long swing-segment. In some cases the dorsal branch of the cephalic vein may also be chosen for the anastomosis which will impose a wide angle anastomosis due to its greater distance from the radial artery. For details on these techniques please refer, e.g., to [56].

4.5. Limitations

We consider blood as a Newtonian fluid in a laminar regime. These assumptions, although they are acceptable in this first FSI study, could be overcome in future works since, due to the small diameter of the vessels and the disturbed flow experienced at the anastomosis, non-Newtonian and turbulence model should be considered.

Regarding the structure problem, the dynamics of both the vessels is modeled using linear elasticity, since the hypothesis of small displacement with respect to the initial configuration is made. Non-linear models such as the Neohookean model or even visco-elastic models could be also adopted.

Concerning the boundary conditions, the radial artery and the cephalic vein are not encapsulated in equal tissue. Since the former lays deeper in the tissues, in a subfascial plane in the wrist, it is more compressed by the external tissues, therefore a further development could be the implementation of the possibility to impose two different values for the Robin coefficient (α_R). Another improvement could be the choice of a more realistic lumped parameter model for the outlet boundary conditions. Instead of a resistance condition, the three-element Windkessel model could be considered. Also, we notice that our inlet boundary conditions were not patient-specific, since Doppler measurements for blood velocity and pressure acquisitions were not available. Future studies could include such information to make the study more realistic.

Finally, we remark that the geometric model is quite simple, since it does not account for nuances and roughness of the lumen surface. However, these are not detectable from standard imaging and we believe they should not influence significantly the blood dynamics (unless one is interested in describing local vortices close to the wall, which is not our case).

5. Conclusion

In the present work we have proposed a FSI model of the end-to-side radio-cephalic arteriovenous fistula to account for the compliance mismatch at the anastomosis. The aim was to understand which anastomosis angle is the best during the first days after the surgical intervention, i.e. when the radial artery and the cephalic vein have still non-negligible geometrical and mechanical differences.

Our results showed that the diameter of the cephalic vein plays a fundamental role in the generation of disturbed flow and abnormal WSS; in particular, a combination of a large diameter of the cephalic vein with a high anastomosis angle seems to create good conditions in terms of vessel stresses and disturbed flow.

CRediT authorship contribution statement

Fabio Marcinnò: Conceptualization, Data curation, Formal analysis, Investigation, Methodology, Software, Writing – original draft, Writing – review & editing. **Christian Vergara:** Conceptualization, Methodology, Project administration, Resources, Supervision, Writing – review & editing. **Luca Giovannacci:** Data curation, Writing – review & editing. **Alfio Quarteroni:** Funding acquisition, Writing – review & editing. **Giorgio Prouse:** Conceptualization, Data curation, Funding acquisition, Investigation, Writing – review & editing.

Declaration of competing interest

The authors have nothing to declare.

Acknowledgements

References

[1] S. Ahmed, I.D. Šutalo, H. Kavnoudias, Hemodynamics and stress distribution in a cerebral aneurysm partially blocked with coils, in: Proceedings of the 5th International Conference on CFD in the Process Industries CSIRO, 2006, pp. 13–15.

[2] A.A. Al-Jaishi, M.J. Oliver, S.M. Thomas, C.E. Lok, J.C. Zhang, A.X. Garg, S.D. Kosa, R.R. Quinn, L.M. Moist, Patency rates of the arteriovenous fistula for hemodialysis: a systematic review and meta-analysis, Am. J. Kidney Dis. 63 (3) (2014) 464–478.

[3] N. Alam, D. Newport, Influence of wall compliance on the flow patterns in a patient-specific brachio-cephalic arterio-venous fistula, Biomechanics 2 (2) (2022) 158–173.

[4] R. Amaya, L.M. Cancel, J.M. Tarbell, Interaction between the stress phase angle (spa) and the oscillatory shear index (osi) affects endothelial cell gene expression, PLoS ONE 11 (11) (2016) e0166569.

[5] L. Antiga, M. Piccinelli, L. Botti, B. Ene-Iordache, A. Remuzzi, D.A. Steinman, An image-based modeling framework for patient-specific computational hemodynamics, Med. Biol. Eng. Comput. 46 (11) (2008) 1097–1112.

[6] R.L. Armentano, L.J. Cymberknop, Mathematical background for mechanical vessel analysis, in: Biomechanical Modeling of the Cardiovascular System, IOP Publishing, 2019, pp. 2053–2563, pp. 3–1 to 3–24.

[7] Z. Bai, L. Zhu, Simulation of blood flow past a distal arteriovenous-graft anastomosis at low Reynolds numbers, Phys. Fluids 31 (9) (2019) 091902.

[8] K. Bashar, M. Clarke-Moloney, P. Burke, E. Kavanagh, S. Walsh, The role of venous diameter in predicting arteriovenous fistula maturation: when not to expect an avf to mature according to pre-operative vein diameter measurements? A best evidence topic, Int. J. Surg. 15 (2015) 95–99.

[9] L. Bennati, C. Vergara, M. Domanin, C. Malloggi, D. Bissacco, S. Trimarchi, V. Silani, G. Parati, R. Casana, A computational fluid–structure interaction study for carotids with different atherosclerotic plaques, J. Biomech. Eng. 143 (9) (2021).

[10] L. Bertagna, S. Deparis, L. Formaggia, D. Forti, A. Veneziani, The lifev library: engineering mathematics beyond the proof of concept, arXiv preprint, arXiv:1710.06596, 2017.

[11] M. Bozzetto, P. Brambilla, S. Rota, B. Ene-Iordache, S. Sironi, G. Remuzzi, A. Remuzzi, Toward longitudinal studies of hemodynamically induced vessel wall remodeling, Int. J. Artif. Organs 41 (11) (2018) 714–722.

[12] M. Bozzetto, B. Ene-Iordache, A. Remuzzi, Transitional flow in the venous side of patient-specific arteriovenous fistulae for hemodialysis, Ann. Biomed. Eng. 44 (8) (2016) 2388–2401.

[13] M. Bozzetto, L. Soliveri, S. Poloni, P. Brambilla, D. Curtò, G.C. Condemi, P. Cefalì, I. Spina, A. Villa, A. Caroli, et al., Arteriovenous fistula creation with vasqtm device: a feasibility study to reveal hemodynamic implications, J. Vasc. Access (2022) 11297298221087160.

[14] M.J. Brescia, J.E. Cimino, K. Appel, B.J. Hurwich, Chronic hemodialysis using venipuncture and a surgically created arteriovenous fistula, N. Engl. J. Med. 275 (20) (1966) 1089–1092.

[15] G.T. Carroll, T.M. McGloughlin, P. Burke, M. Egan, F. Wallis, M.T. Walsh, Wall shear stresses remain elevated in mature arteriovenous fistulas: a case study, J. Biomech. Eng. 133 (2) (2011).

[16] A. Chandra, D. Mix, N. Varble, Hemodynamic study of arteriovenous fistulas for hemodialysis access, Vascular 21 (1) (2013) 54–62.

[17] X. Chen, Y. Gao, B. Lu, X. Jia, L. Zhong, G.S. Kassab, W. Tan, Y. Huo, Hemodynamics in coronary arterial tree of serial stenoses, PLoS ONE 11 (9) (2016) e0163715.

[18] E. Colley, J. Carroll, S. Anne, T. Shannon, V. Ramon, B. Tracie, A longitudinal study of the arterio-venous fistula maturation of a single patient over 15 weeks, Biomech. Model. Mechanobiol. 21 (4) (2022) 1217–1232.

[19] E. Colley, A. Simmons, R. Varcoe, S. Thomas, T. Barber, Arteriovenous fistula maturation and the influence of fluid dynamics, Proc. Inst. Mech. Eng., H J. Eng. Med. 234 (11) (2020) 1197–1208.

[20] P.C. de Groot, M.W. Bleeker, M.T. Hopman, Ultrasound: a reproducible method to measure conduit vein compliance, J. Appl. Physiol. 98 (5) (2005) 1878–1883.

[21] A. de Villiers, A. McBride, B. Reddy, T. Franz, B. Spottiswoode, A validated patient-specific fsi model for vascular access in haemodialysis, Biomech. Model. Mechanobiol. 17 (2) (2018) 479–497.

[22] I. Decorato, Z. Kharboutly, C. Legallais, A.-V. Salsac, Comparison of two endovascular treatments of a stenosed arteriovenous fistula: balloon-angioplasty with and without stenting, Int. J. Artif. Organs 37 (10) (2014) 763–772.

[23] I. Decorato, Z. Kharboutly, T. Vassallo, J. Penrose, C. Legallais, A.-V. Salsac, Numerical simulation of the fluid structure interactions in a compliant patient-specific arteriovenous fistula, Int. J. Numer. Methods Biomed. Eng. 30 (2) (2014) 143–159.

[24] S. Deparis, D. Forti, P. Gervasio, A. Quarteroni, Internodes: an accurate interpolation-based method for coupling the Galerkin solutions of pdes on subdomains featuring non-conforming interfaces, Comput. Fluids 141 (2016) 22–41.

[25] S. Deparis, D. Forti, G. Grandperrin, A. Quarteroni, Facsi: a block parallel preconditioner for fluid–structure interaction in hemodynamics, J. Comput. Phys. 327 (2016) 700–718.

[26] S. Deparis, D. Forti, A. Quarteroni, A fluid–structure interaction algorithm using radial basis function interpolation between non-conforming interfaces, in: Advances in Computational Fluid-Structure Interaction and Flow Simulation: New Methods and Challenging Computations, 2016, p. 439.

[27] B. Ene-Iordache, L. Cattaneo, G. Dubini, A. Remuzzi, Effect of anastomosis angle on the localization of disturbed flow in 'side-to-end'fistulae for haemodialysis access, Nephrol. Dial. Transplant. 28 (4) (2013) 997–1005.

[28] B. Ene-Iordache, A. Remuzzi, Disturbed flow in radial-cephalic arteriovenous fistulae for haemodialysis: low and oscillating shear stress locates the sites of stenosis, Nephrol. Dial. Transplant. 27 (1) (2012) 358–368.

[29] B. Ene-Iordache, C. Semperboni, G. Dubini, A. Remuzzi, Disturbed flow in a patient-specific arteriovenous fistula for hemodialysis: multidirectional and reciprocating near-wall flow patterns, J. Biomech. 48 (10) (2015) 2195–2200.

[30] F. Fahrtash, L. Kairaitis, S. Gruenewald, T. Spicer, H. Sidrak, J. Fletcher, R. Allen, J. Swinnen, Defining a significant stenosis in an autologous radio-cephalic arteriovenous fistula for hemodialysis, in: Seminars in Dialysis, vol. 24, Wiley Online Library, 2011, pp. 231–238.

[31] M. Fedele, A. Quarteroni, Polygonal surface processing and mesh generation tools for the numerical simulation of the cardiac function, Int. J. Numer. Methods Biomed. Eng. 37 (4) (2021) e3435.

[32] D.E. Finlay, D.G. Longley, M.C. Foshager, J.G. Letourneau, Duplex and color Doppler sonography of hemodialysis arteriovenous fistulas and grafts, Radiographics 13 (5) (1993) 983–989.

[33] L. Formaggia, A. Quarteroni, A. Veneziani, Cardiovascular Mathematics: Modeling and Simulation of the Circulatory System, vol. 1, Springer Science & Business Media, 2010.

[34] L. Formaggia, C. Vergara, Prescription of general defective boundary conditions in fluid-dynamics, Milan J. Math. 80 (2) (2012) 333–350.

[35] D. Forti, M. Bukac, A. Quaini, S. Canic, S. Deparis, A monolithic approach to fluid–composite structure interaction, J. Sci. Comput. 72 (1) (2017) 396–421.

[36] D. Forti, L. Dedè, Semi-implicit bdf time discretization of the Navier–Stokes equations with vms-les modeling in a high performance computing framework, Comput. Fluids 117 (2015) 168–182.

[37] J. Gameiro, J. Ibeas, Factors affecting arteriovenous fistula dysfunction: a narrative review, J. Vasc. Access 21 (2) (2020) 134–147.

[38] D. Getachew, A. Astatkie, K. Lemma, Diameter, vessel thickness and angle of bifurcation of the radial artery in Ethiopian cadavers, J. Morphol. Sci. 35 (02) (2018) 129–135.

[39] C. Geuzaine, J.-F. Remacle, Gmsh: a 3-d finite element mesh generator with built-in pre-and post-processing facilities, Int. J. Numer. Methods Eng. 79 (11) (2009) 1309–1331.

[40] W. Guess, B. Reddy, A. McBride, B. Spottiswoode, J. Downs, T. Franz, Fluid-structure interaction modelling and stabilisation of a patient-specific arteriovenous access fistula, arXiv preprint, arXiv:1704.07753, 2017.

[41] M. Jahangiri, M. Saghafian, M.R. Sadeghi, Numerical study of turbulent pulsatile blood flow through stenosed artery using fluid-solid interaction, in: Computational and Mathematical Methods in Medicine 2015, 2015.

[42] M.F. Kheda, L.E. Brenner, M.J. Patel, J.J. Wynn, J.J. White, L.M. Prisant, S.A. Jones, W.D. Paulson, Influence of arterial elasticity and vessel dilatation on arteriovenous fistula maturation: a prospective cohort study, Nephrol. Dial. Transplant. 25 (2) (2010) 525–531.

[43] A. Kordzadeh, J. Chung, Y.P. Panayiotopoulos, Cephalic vein and radial artery diameter in formation of radiocephalic arteriovenous fistula: a systematic review, J. Vasc. Access 16 (6) (2015) 506–511.

[44] R.M. Lancellotti, C. Vergara, L. Valdettaro, S. Bose, A. Quarteroni, Large eddy simulations for blood dynamics in realistic stenotic carotids, Int. J. Numer. Methods Biomed. Eng. 33 (11) (2017) e2868.

[45] S. Laurent, X. Girerd, J.-J. Mourad, P. Lacolley, L. Beck, P. Boutouyrie, J.-P. Mignot, M. Safar, Elastic modulus of the radial artery wall material is not increased in patients with essential hypertension, Arterioscler. Thromb. Vasc. Biol. 14 (7) (1994) 1223–1231.

[46] J. Liu, W. Yang, I.S. Lan, A.L. Marsden, Fluid-structure interaction modeling of blood flow in the pulmonary arteries using the unified continuum and variational multi-scale formulation, Mech. Res. Commun. 107 (2020) 103556.

[47] C. Long, M.-C. Hsu, Y. Bazilevs, J. Feinstein, A. Marsden, Fluid–structure interaction simulations of the fontan procedure using variable wall properties, Int. J. Numer. Methods Biomed. Eng. 28 (5) (2012) 513–527.

[48] MATLAB, version R2022a, The MathWorks Inc., Natick, Massachusetts, 2022.

[49] P.M. McGah, D.F. Leotta, K.W. Beach, A. Aliseda, Effects of wall distensibility in hemodynamic simulations of an arteriovenous fistula, Biomech. Model. Mechanobiol. 13 (3) (2014) 679–695.

[50] A. McNally, A.G. Akingba, P. Sucosky, Effect of arteriovenous graft flow rate on vascular access hemodynamics in a novel modular anastomotic valve device, J. Vasc. Access 19 (5) (2018) 446–454.

[51] A.Y. Mousa, D.D. Dearing, A.F. AbuRahma, Radiocephalic fistula: review and update, Ann. Vasc. Surg. 27 (3) (2013) 370–378.

[52] US Renal Data System. 2020 United States Renal Data System (USRDS) Annual Data Report: Epidemiology of Kidney Disease in the United States. National Institutes of Health, National Institute of Diabetes and Digestive and Kidney Diseases, 2020.

[53] F. Nobile, M. Pozzoli, C. Vergara, Time accurate partitioned algorithms for the solution of fluid–structure interaction problems in haemodynamics, Comput. Fluids 86 (2013) 470–482.

[54] A. Ochsner Jr, R. Colp Jr, G. Burch, Normal blood pressure in the superficial venous system of man at rest in the supine position, Circulation 3 (5) (1951) 674–680.

[55] M. Piccinelli, C. Vergara, L. Antiga, L. Forzenigo, P. Biondetti, M. Domanin, Impact of hemodynamics on lumen boundary displacements in abdominal aortic aneurysms by means of dynamic computed tomography and computational fluid dynamics, Biomech. Model. Mechanobiol. 12 (6) (2013) 1263–1276.

[56] G. Prouse, S. Stella, C. Vergara, A. Quarteroni, S. Engelberger, R. Canevascini, L. Giovannacci, Computational analysis of turbulent hemodynamics in radiocephalic arteriovenous fistulas to determine the best anastomotic angles, Ann. Vasc. Surg. 68 (2020) 451–459.

[57] A. Quarteroni, A. Manzoni, C. Vergara, The cardiovascular system: mathematical modelling, numerical algorithms and clinical applications, Acta Numer. 26 (2017) 365–590.

[58] A. Quarteroni, A. Veneziani, C. Vergara, Geometric multiscale modeling of the cardiovascular system, between theory and practice, Comput. Methods Appl. Mech. Eng. 302 (2016) 193–252.

[59] K.B. Quencer, M. Arici, Arteriovenous fistulas and their characteristic sites of stenosis, Am. J. Roentgenol. 205 (4) (2015) 726–734.

[60] S. Quicken, Y. de Bruin, B. Mees, J. Tordoir, T. Delhaas, W. Huberts, Computational study on the haemodynamic and mechanical performance of electrospun polyurethane dialysis grafts, Biomech. Model. Mechanobiol. 19 (2) (2020) 713–722.

[61] P.J. Roache, Quantification of uncertainty in computational fluid dynamics, Annu. Rev. Fluid Mech. 29 (1) (1997) 123–160.

[62] M.L. Robbin, T. Greene, A.K. Cheung, M. Allon, S.A. Berceli, J.S. Kaufman, M. Allen, P.B. Imrey, M.K. Radeva, Y.-T. Shiu, et al., Arteriovenous fistula development in the first 6 weeks after creation, Radiology 279 (2) (2016) 620–629.

[63] M. Sadeghi, E. Shirani, M. Tafazzoli-Shadpour, M. Samaee, The effects of stenosis severity on the hemodynamic parameters—assessment of the correlation between stress phase angle and wall shear stress, J. Biomech. 44 (15) (2011) 2614–2626.

[64] W. Schnell, Westergaard, hm-theory of elasticity and plasticity, 1966.

[65] S.N. Shembekar, D. Zodpe, P.M. Padole, Fluid-structure interaction of pulsatile flow within the flexible wall radio-cephalic arteriovenous fistula, Available at SSRN 4044568, 2022.

[66] S. Sivanesan, T.V. How, A. Bakran, Sites of stenosis in av fistulae for haemodialysis access, Nephrol. Dial. Transplant. 14 (1) (1999) 118–120.

[67] P. Skacel, J. Bursa, Poisson's ratio and compressibility of arterial wall–improved experimental data reject auxetic behaviour, J. Mech. Behav. Biomed. Mater. 131 (2022) 105229.

[68] S. Stella, C. Vergara, L. Giovannacci, A. Quarteroni, G. Prouse, Assessing the disturbed flow and the transition to turbulence in the arteriovenous fistula, J. Biomech. Eng. 141 (10) (2019).

[69] T.E. Tezduyar, Stabilized finite element formulations for incompressible flow computations, Adv. Appl. Mech. 28 (1991) 1–44.

[70] J. van der Linden, T.W. Lameris, A.H. van den Meiracker, A.A. de Smet, P.J. Blankestijn, M.A. van den Dorpel, Forearm venous distensibility predicts successful arteriovenous fistula, Am. J. Kidney Dis. 47 (6) (2006) 1013–1019.

[71] I. Van Tricht, D. De Wachter, J. Tordoir, P. Verdonck, Hemodynamics and complications encountered with arteriovenous fistulas and grafts as vascular access for hemodialysis: a review, Ann. Biomed. Eng. 33 (2005) 1142–1157.

[72] Y. Yang, Analysis of personalized mechano-bio-faithful radio-cephalic arteriovenous Fistula, PhD thesis, Université de Lyon, 2021.

[73] F. Zhang, Y. Li, T. Wang, J. Tao, J. Zhu, M. Wei, L. Mo, X. Li, Y. Wang, Y. Cheng, Influence of cephalic vein dilation on arteriovenous fistula maturation in patients with small cephalic veins, Medicine 99 (1) (2020).